

Chaos for a Microelectromechanical Oscillator Governed by the Nonlinear Mathieu Equation

Barry E. DeMartini, *Student Member, IEEE*, Holly E. Butterfield, *Student Member, ASME*,
Jeff Moehlis, and Kimberly L. Turner, *Member, IEEE, Member, ASME*

Abstract—A variety of microelectromechanical (MEM) oscillators is governed by a version of the Mathieu equation that harbors both linear and cubic nonlinear time-varying stiffness terms. In this paper, chaotic behavior is predicted and shown to occur in this class of MEM device. Specifically, by using Melnikov's method, an inequality that describes the region of parameter space where chaos lives is derived. Numerical simulations are performed to show that chaos indeed occurs in this region of parameter space and to study the system's behavior for a variety of parameters. A MEM oscillator utilizing noninterdigitated comb drives for actuation and stiffness tuning was designed and fabricated, which satisfies the inequality. Experimental results for this device that are consistent with results from numerical simulations are presented and convincingly show chaotic behavior. [2006-0281]

Index Terms—Chaos, electrostatic actuation, Melnikov's method, noninterdigitated comb drives, nonlinear, parametric resonators, tuning.

I. INTRODUCTION

A CLASS OF nonlinear parametrically excited microelectromechanical (MEM) oscillators has recently garnered much attention in the research community. Due to the abrupt changes in dynamic behavior (nearly instantaneous jumps from a stable quiescent state to a stable oscillatory state), parametrically excited oscillators are attractive for applications such as filtering [1], [2], mass sensing [3], [4], and scanning probe microscopy [5]. A thorough analysis of the governing equation of motion has provided an accurate model of the dynamic response of such devices [6]–[8], which has compared well with experimental results. Characteristic to this class of oscillators is the presence of linear and cubic nonlinear time-varying stiffness coefficients that arise due to electrostatic forces produced by noninterdigitated comb drives (as will be discussed further in the following sections). This governing equation is a nonlinear version of the well-known

Mathieu equation, which conventionally contains only linear time-varying coefficients [9].

In recent work, a novel tuning technique for such oscillators has been developed [2], [10]–[12]. Such oscillators consist of two sets of noninterdigitated comb fingers. An ac signal is applied to one comb drive set to provide a time- and displacement-dependent force that drives the device. To the second set, a dc voltage is applied to tune the effective linear and nonlinear stiffness of the device. Of interest in this study are tunable MEM oscillators that are governed by the same equation as in Rhoads *et al.* [6]. Specifically, we will analyze the chaotic behavior for such a device.

Chaotic behavior has been discovered and reported for many physical systems. A classical example of a chaotic system is the Lorenz equations [13], which were derived to help understand the dynamics of cellular convection. Chaos due to various mechanisms has also been reported for nonlinear MEM oscillators, including microcantilevers for atomic force microscopy [14]–[18], an in-plane MEM oscillator with separated comb drive actuators for signal encryption applications [19], an electrostatically actuated MEM cantilever control system [20], and MEM oscillators based on variable gap capacitors [21], [22]. To the authors' knowledge, the presence of chaos has not been thoroughly investigated for the Mathieu oscillators with time-varying linear and nonlinear stiffness terms discussed previously.

Knowledge of the conditions that cause such behavior to occur is important both for creating devices that exploit chaotic vibrations for signal encryption applications and for creating robust devices with predictable dynamic behavior. Here, Melnikov's method [23] has been employed to define the regions of parameter space where homoclinic chaos can occur. Numerical analysis was used to study the system's behavior for various parameter sets and to verify the result from Melnikov's method. Finally, a MEM oscillator was designed and fabricated such that for a range of applied voltages and driving frequencies chaos is predicted to occur from Melnikov's method. The chaotic behavior of this device was verified experimentally using a laser vibrometer.

In Section II, the governing dynamics of the oscillator of interest are presented. A general discussion of Melnikov's method and how it can be used to predict chaotic behavior in nonlinear MEM oscillators is presented in Section III. Then, in Section IV Melnikov's method is applied to the MEM oscillator of interest, ultimately yielding a criterion for chaotic behavior to occur, and numerical results are presented and discussed. In Section V, experimental results for a fabricated MEM system

Manuscript received December 18, 2006; revised July 25, 2007. This work was supported by the National Science Foundation under Grant NSF-0428916 and Grant NSF-0547606. Subject Editor N. Aluru.

B. E. DeMartini, J. Moehlis, and K. L. Turner are with the Department of Mechanical Engineering, University of California, Santa Barbara, CA 93106 USA (e-mail: baredog@enr.ucsb.edu; moehlis@enr.ucsb.edu; turner@enr.ucsb.edu).

H. E. Butterfield was with the Department of Mechanical Engineering, University of California, Santa Barbara, CA 93106 USA. She is now with the Department of Mechanical Engineering, Stanford University, Stanford, CA 94305 USA (e-mail: heb@stanford.edu).

Digital Object Identifier 10.1109/JMEMS.2007.906757

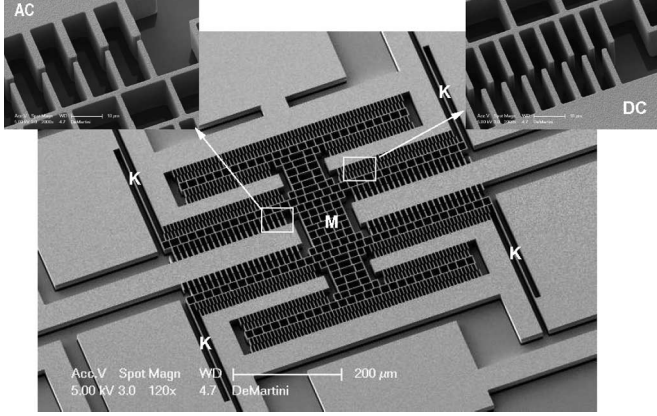


Fig. 1. SEM image of the MEM oscillator consisting of a proof mass (M), mechanical flexures (K), a driving set of ac noninterdigitated comb fingers (AC), and a tuning set of dc noninterdigitated comb fingers (DC).

showing convincing chaotic vibrations are presented and discussed. Finally, we conclude in Section VI.

II. DYNAMICS OF A MEM OSCILLATOR GOVERNED BY THE NONLINEAR MATHIEU EQUATION

The layout of the oscillator that was studied is shown in Fig. 1, where M is the oscillator's backbone (or proof mass), AC and DC are noninterdigitated comb drive actuators, and K are flexures. A square root cosine voltage signal $V(t) = V_A \sqrt{1 + \cos(\omega t)}$, which decouples parametric and harmonic excitation [5], is applied to the ac actuators. For tuning purposes, a dc voltage V_0 is applied to the dc actuators. The electrostatic force generated by these actuators, which has been previously studied and validated via numerical simulation, finite-element analysis, and experimental investigation [3], [10], is described by

$$F_{es}(x, t) = (r_{10}x + r_{30}x^3) V_0^2 + (r_{1A}x + r_{3A}x^3) V_A^2 (1 + \cos \omega t) \quad (1)$$

where r_{10} and r_{30} are, respectively, the linear and cubic nonlinear electrostatic stiffness of the dc comb fingers, and r_{1A} and r_{3A} are, respectively, the linear and cubic nonlinear electrostatic stiffness of the ac comb fingers. A unique feature of this type of electrostatic actuator is that the stiffness coefficients (r_{10} , r_{30} , r_{1A} , and r_{3A}) can be positive or negative depending on the geometry and alignment of the comb fingers [10], [12]. As an example, if the comb fingers are aligned with one another for a given set of dimensions, then the linear electrostatic stiffness could be positive and the nonlinear stiffness could be negative. On the other hand, if the comb fingers are misaligned, then the linear electrostatic stiffness could be negative and the nonlinear stiffness could be positive. The dimensions of these fingers will also strongly affect the magnitude and sign of these coefficients. The mechanical flexures provide a restoring force to the system that is described by

$$F_r(x) = k_1x + k_3x^3 \quad (2)$$

TABLE I
DERIVATIVE OPERATOR AND NONDIMENSIONAL
PARAMETER DEFINITIONS

$' = d/d\tau$	derivative operator
$\alpha = c/(\omega_0 m)$	damping coefficient
$\beta = 1 + r_{10}V_0^2/k_1$	tunable linear stiffness
$\delta = x_0^2(k_3 + r_{30}V_0^2)/k_1$	tunable nonlinear stiffness
$\gamma = r_{1A}V_A^2/k_1$	linear electrostatic stiffness coefficient
$\eta = x_0^2r_{3A}V_A^2/k_1$	nonlinear electrostatic stiffness coefficient

where k_1 is the linear mechanical stiffness and k_3 is the cubic nonlinear mechanical stiffness that arises due to boundary conditions that impart stress on the neutral axis of each flexure (note that $k_3 > 0$ due to the natural hardening nature of the beams). Including a dissipative force due to linear viscous damping, the equation of motion for this system becomes

$$m\ddot{x} + c\dot{x} + k_1x + k_3x^3 + (r_{10}x + r_{30}x^3) V_0^2 + (r_{1A}x + r_{3A}x^3) V_A^2 (1 + \cos \omega t) = 0 \quad (3)$$

where m is the mass, and c is the damping coefficient. Equation (3) is a nonlinear version of the Mathieu equation and is valid provided that the shuttle mass moves primarily in one direction (i.e., no other modes of oscillation affect the motion of the oscillator), that the aligned comb fingers remain approximately aligned and misaligned comb fingers remain approximately misaligned during oscillation (this is discussed for a tested device in Section V), and that the dominant source of damping in the system is due to viscous effects and is linear (this dynamic model was previously studied and validated for a similar device in [3], [6], and [7]).

For analytical purposes, time in (3) is rescaled as $\tau = \omega_0 t$, where $\omega_0 = \sqrt{k_1/m}$ is the system's pure elastic linear natural frequency, and displacement is rescaled as $z = x/x_0$, where x_0 is a characteristic length (e.g., the center-to-center distance between comb fingers). The ratio of the driving frequency to the natural frequency is defined to be $\Omega = \omega/\omega_0$. Rearranging, the nondimensionalized equation of motion becomes

$$z'' + \alpha z' + \beta z + \delta z^3 + \gamma(1 + \cos \Omega\tau)z + \eta(1 + \cos \Omega\tau)z^3 = 0 \quad (4)$$

where the new derivative operator and nondimensional parameters are defined in Table I.

III. MELNIKOV'S METHOD AND CHAOS

Melnikov's method is an analytical technique, which can be used to deduce the presence of chaos in a dynamical system.

Consider the general one degree of freedom system [23], i.e.,

$$\dot{x} = f_0(x, y) + \epsilon g_0(x, y, t) = \frac{\partial H}{\partial y} + \epsilon g_0(x, y, t) \quad (5)$$

$$\dot{y} = f_1(x, y) + \epsilon g_1(x, y, t) = -\frac{\partial H}{\partial x} + \epsilon g_1(x, y, t) \quad (6)$$

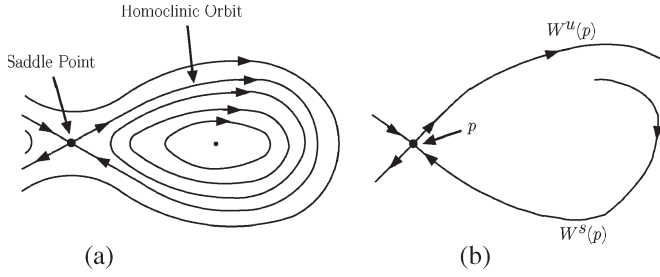


Fig. 2. (a) Phase space for the unperturbed system ($\epsilon = 0$) that contains a saddle point, homoclinic trajectories, and periodic orbits. (b) Phase space for the Poincaré map when a perturbation ($\epsilon \neq 0$) is applied where the stable manifold $W^s(p)$ and unstable manifold $W^u(p)$ separate.

where ϵ is a small parameter, g is periodic in t with period T , and H is a real Hamiltonian function. Suppose that for the unperturbed ($\epsilon = 0$) autonomous system, a saddle point with overlapping stable and unstable manifolds exists, corresponding to a homoclinic orbit [see Fig. 2(a)]. When a small perturbation is applied (i.e., $\epsilon \neq 0$), there will be a periodic orbit close to the saddle point, which will be a fixed point p of the Poincaré map defined by evolution for a time T (i.e., a point in phase space is recorded once every period T). The stable and unstable manifolds ($W^s(p)$ and $W^u(p)$, respectively) of p will be close to their counterparts for the saddle point for the unperturbed system, but the homoclinic orbit will typically be broken, so that $W^s(p)$ and $W^u(p)$ no longer lie on top of one another [see Fig. 2(b)]. By Moser's theorem and the Smale–Birkhoff homoclinic theorem, if the stable and unstable manifolds intersect transversely then the system's dynamics will contain a horseshoe [24]. The existence of a horseshoe implies that there is a countable infinity of periodic orbits, an uncountable number of aperiodic orbits, and a dense orbit, which comes arbitrarily close to every point in the invariant set of the horseshoe map. In other words, a chaotic set exists in the system when a transverse intersection of the manifolds occurs. We emphasize that this set is not necessarily an attractor.

The Melnikov function gives a measure of the leading order distance between the stable and unstable manifolds when $\epsilon \neq 0$ and can be used to tell when the stable and unstable manifolds intersect transversely. It is defined to be the integral

$$M(t_0) = \int_{-\infty}^{\infty} [f_0(x_0, y_0)g_1(x_0, y_0, t + t_0) - f_1(x_0, y_0)g_0(x_0, y_0, t + t_0)] dt \quad (7)$$

where $q^0(t) = (x_0, y_0)$ is the solution corresponding to the unperturbed homoclinic trajectory. If $M(t_0) = 0$ and $M'(t_0) \neq 0$ for some t_0 and some set of parameters then the two manifolds have a transverse intersection, a horseshoe exists, and chaos occurs [23]. Melnikov's method can serve as a useful tool in the development of nonlinear MEM oscillators, giving bounds on the parameters of a system where chaos, resulting from such intersections, can occur.

IV. APPLICATION TO A MEM OSCILLATOR GOVERNED BY A NONLINEAR VERSION OF THE MATHIEU EQUATION

A. Scaling and Conditions for Homoclinic Trajectories

In order to perform Melnikov analysis on (4), some rescaling is performed. Specifically, (4) needs to be rewritten to take the same form as (5) and (6). The following parameters corresponding to time-dependent and velocity terms (i.e., forcing and damping) are assumed to be small:

$$\alpha \equiv \epsilon\tilde{\alpha} = \mathcal{O}(\epsilon) \quad \gamma \equiv \epsilon\tilde{\gamma} = \mathcal{O}(\epsilon) \quad \eta \equiv \epsilon\tilde{\eta} = \mathcal{O}(\epsilon) \quad (8)$$

which is a valid assumption for MEM oscillators. All other time-independent terms are assumed to be first-order quantities [i.e., $\beta = \mathcal{O}(1)$, $\delta = \mathcal{O}(1)$]. Defining $z' = v$ and rewriting the second-order differential equation as two first-order differential equations gives the following perturbed system:

$$\begin{aligned} z' &= v \\ v' &= -\beta z - \delta z^3 \\ &+ \epsilon [-\tilde{\alpha}v - \tilde{\gamma}(1 + \cos(\Omega\tau))z - \tilde{\eta}(1 + \cos(\Omega\tau))z^3]. \end{aligned} \quad (9)$$

For the unperturbed ($\epsilon = 0$) system, the following Hamiltonian is found:

$$H(z, v) = \frac{1}{2}v^2 + \frac{1}{2}\beta z^2 + \frac{1}{4}\delta z^4. \quad (10)$$

From this Hamiltonian, the following conditions are placed on parameters so that the Hamiltonian exhibits a double-well structure and, hence, has a homoclinic trajectory:

$$\beta < 0 \quad \delta > 0. \quad (11)$$

The energy of the system can be visualized by plotting the potential energy portion of (10), i.e., $U(z) = \beta z^2/2 + \delta z^4/4$, as a function of displacement z , as shown in Fig. 3(a). For $\beta = 0$, the potential energy is at a bifurcation point where it has not quite reached a double-well state [dotted curve in Fig. 3(a)] and is a symmetric quartic curve. As V_0 is increased past the critical value $V_{0,\text{crit}}^\beta$, two wells (minima) are created, which can be thought of as stable fixed points, and the fixed point at the origin becomes unstable. By treating V_0 as a bifurcation parameter and plotting the position of each equilibrium point (the maxima and minimum of the potential energy), Fig. 3(b) is generated, which is the well-known pitchfork bifurcation. In an experiment, small noise-induced perturbations cause the device to leave the unstable origin and settle to one of the two stable positions when $V_0 > V_{0,\text{crit}}^\beta$. By only activating the dc comb drives and observing the device snap to a new equilibrium position, this behavior can be exploited to verify condition (11) prior to exploring the chaotic dynamics, as will be done in the succeeding sections.

From (11), to obtain chaos the main obstacle that needs to be overcome in the design process is to create a net negative linear stiffness, i.e., $\beta < 0$. To overcome this seemingly unphysical condition, the dc comb fingers can be chosen to have a large negative linear stiffness, so that under reasonable V_0 the net

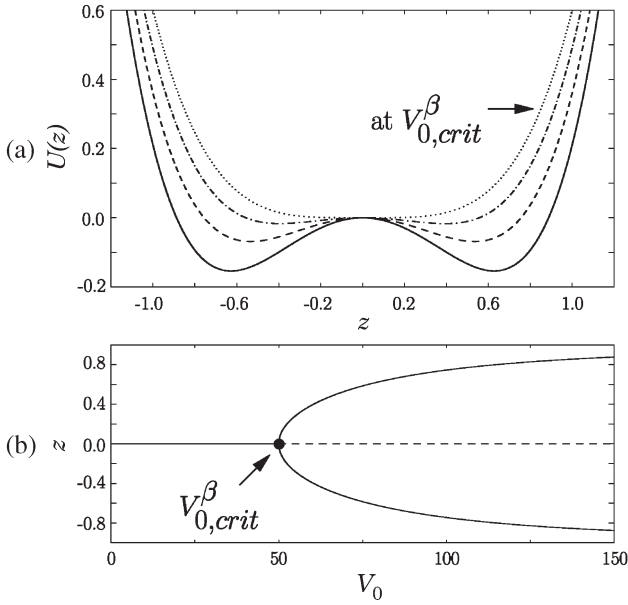


Fig. 3. Representative figures for $\epsilon = 0$ and $\delta > 0$, showing the (a) potential energy $U(z) = (1/2)\beta z^2 + (1/4)\delta z^4$ with $\beta \leq 0$, as a function of displacement z , illustrating the system's double-well structure (dotted curve represents $V_0 = V_{0,crit}^\beta$, and all other curves represent the case when $V_0 > V_{0,crit}^\beta$, where the solid curve represents the highest V_0) and (b) bifurcation diagram showing the position of each extremum as a function of V_0 (solid curves give stable solutions, and dashed curves give unstable solutions).

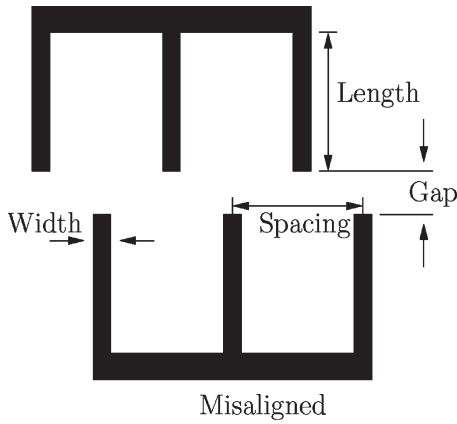


Fig. 4. Geometry of misaligned noninterdigitated comb drives proposed for tuning the oscillator such that $\beta < 0$ and $\delta > 0$.

stiffness β is negative. Various aspects of the comb finger and flexure design are discussed in Section IV-B.

B. Design Considerations

In order to create a MEM oscillator satisfying (11), the dc tuning comb drives [10]–[12] and flexures must be designed accordingly. Since $\beta \sim k_1 + r_{10}V_0^2$ and k_1 is always positive, the tuning comb drives need to be configured so that $r_{10} < 0$. This is achieved by making the comb fingers misaligned with respect to one another (see Fig. 4). Furthermore, V_0 must be larger than the following critical voltage

$$V_{0,crit}^\beta = \sqrt{-k_1/r_{10}} \quad (12)$$

to achieve $\beta < 0$. To decrease this critical voltage, the oscillator can be designed with small k_1 and large r_{10} . Long thin flexures can be used to reduce k_1 .

The other critical coefficient is $\delta \sim k_3 + r_{30}V_0^2$. Since k_3 is always positive, r_{30} can either be positive or negative to satisfy $\delta > 0$. Although it is preferable to design $r_{30} > 0$ so that $\delta > 0$ for all V_0 , if $r_{30} < 0$ one can still satisfy $\delta > 0$ by taking V_0 less than the critical voltage, i.e.,

$$V_{0,crit}^\delta = \sqrt{-k_3/r_{30}}. \quad (13)$$

In this case by designing k_3 as large and r_{30} as small, the upper bound $V_{0,crit}^\delta$ is increased. To increase the magnitude of k_3 , fixed-fixed flexures, which are shown in Fig. 1 as beams labeled K, can be used.

The magnitudes of r_{10} and r_{30} can be increased by increasing the number of comb fingers and changing their dimensions. One way to achieve this is by decreasing the gap between the comb fingers. In addition, increasing the spacing between each finger will make r_{30} more positive. The effects of geometry on these parameters can be explored using finite-element software and have been previously documented [10]–[12].

C. Applying Melnikov's Method

Satisfying the conditions for a double-well potential gives rise to a homoclinic orbit in the system's phase space for $\epsilon = 0$. The homoclinic trajectory can be found by setting $H(z, v) = 0$. Solving for the resulting displacement and differentiating to determine velocity, the homoclinic trajectory is given as follows [23]:

$$z_0(\tau) = \pm \sqrt{2|\beta|/\delta} \operatorname{sech}(\sqrt{|\beta|}\tau), \quad (14)$$

$$v_0(\tau) = \mp |\beta|\sqrt{2/\delta} \operatorname{sech}(\sqrt{|\beta|}\tau) \tanh(\sqrt{|\beta|}\tau). \quad (15)$$

The Melnikov function (7) can now be evaluated, where $f_0(z, v) = v$, $g_0(z, v, \tau) = 0$, and

$$f_1(z, v) = -\beta z - \delta z^3$$

$$g_1(z, v, \tau) = -\tilde{\alpha}v - \tilde{\gamma}(1 + \cos(\Omega\tau))z - \tilde{\eta}(1 + \cos(\Omega\tau))z^3. \quad (16)$$

The integral becomes

$$M(\tau_0) = \int_{-\infty}^{\infty} v_0(\tau) [-\tilde{\alpha}z'_0(\tau) - \tilde{\gamma}(1 + \cos(\Omega(\tau + \tau_0)))z_0(\tau) - \tilde{\eta}(1 + \cos(\Omega(\tau + \tau_0)))(z_0(\tau))^3] d\tau \quad (17)$$

which yields

$$M(\tau_0) = \kappa [\pi\Omega^2 (6\delta\tilde{\gamma} + \tilde{\eta}(4|\beta| + \Omega^2)) \sin(\Omega\tau_0) + 8\tilde{\alpha}|\beta|^{\frac{3}{2}}\delta \sinh(\pi\Omega/(2\sqrt{|\beta|}))] \quad (18)$$

where $\kappa = -\operatorname{csch}(\pi\Omega/(2\sqrt{|\beta|}))/(\delta\delta^2)$. In order for the unstable and stable manifolds to intersect, Melnikov's method states

TABLE II
PHYSICAL PARAMETERS OF A REPRESENTATIVE DEVICE
STUDIED USING NUMERICAL ANALYSIS

k_1	$5\mu\text{N}/\mu\text{m}$
k_3	$7\mu\text{N}/\mu\text{m}^3$
m	$3 \times 10^{-10}\text{kg}$
c	$1.9 \times 10^{-8}\text{kg/s}$
r_{10}	$-2 \times 10^{-3}\mu\text{N}/(\text{V}^2\mu\text{m})$
r_{30}	$2 \times 10^{-3}\mu\text{N}/(\text{V}^2\mu\text{m}^3)$
r_{1A}	$1 \times 10^{-3}\mu\text{N}/(\text{V}^2\mu\text{m})$
r_{3A}	$-4 \times 10^{-4}\mu\text{N}/(\text{V}^2\mu\text{m}^3)$

that $M(\tau_0) = 0$ for some τ_0 . For this to hold, the following criterion must be met:

$$Y(\Omega) \equiv \left| 8\alpha|\beta|^{\frac{3}{2}}\delta \sinh\left(\frac{\pi\Omega}{2\sqrt{|\beta|}}\right) \right| - \left| \pi\Omega^2(6\delta\gamma + \eta(4|\beta| + \Omega^2)) \right| < 0. \quad (19)$$

Consequently, an oscillator whose parameters satisfy this expression will have a chaotic invariant set, which may or may not be an attractor. It is important to note that a large region of parameter space will satisfy this inequality.

D. Numerical Analysis of a Realistic MEM Oscillator

For the purposes of this analysis, realistic parameters are chosen based on an electrostatically driven Mathieu MEM oscillator presented in DeMartini *et al.* [12]; these are shown in Table II. (Note that these are not the exact parameters of that device, rather they were chosen as representative values for a device that can be designed and manufactured.) This particular device is chosen for this study because it satisfies the aforementioned homoclinic trajectory criterion, i.e., $\beta < 0$ and $\delta > 0$. Since $r_{30} > 0$, $\delta > 0$ will be true for all V_0 , and $V_0 > V_{0,\text{crit}}^\beta$ will therefore be the critical condition in this analysis. It turns out that $V_{0,\text{crit}}^\beta = 50$ V for these parameters. In [12], the second set of comb fingers, used to drive the oscillator, are aligned relative to one another giving rise to $r_{1A} > 0$ and $r_{3A} < 0$. The driving voltage V_A can be used to tune the parameters γ and η to satisfy (19). It is important to note that by choosing different comb finger arrangements for actuation, e.g., misaligned comb fingers where $r_{1A} > 0$ and $r_{3A} < 0$, Melnikov's criterion can still be satisfied. The aligned arrangement is chosen simply for comparison with the work in [12]. Having the set of representative parameters, numerical analysis is performed to study the system and to verify that (19) does in fact describe the set of parameters where chaos occurs.

Depending on the magnitude of the ac and dc voltages chosen, α , β , δ , γ , and η can be tuned to satisfy (19). As an example, choosing $V_0 = 75$ V, $V_A = 40$ V, and setting $x_0 = 1$ yields $\alpha = 0.0005$, $\beta = -1.25$, $\delta = 3.65$, $\gamma = 0.32$, and $\eta = -0.128$, which not only satisfy (19) for a certain range of Ω but are also consistent with the aforementioned scaling assumptions and requirements on β and δ . The function $Y(\Omega)$ is plotted in Fig. 5. Chaos is predicted to occur for the band of Ω where $Y(\Omega) < 0$. For example consider the solid curve in Fig. 5(a), where $V_A = 40$ V and $V_0 = 75$ V; for this parameter set, chaos is predicted to occur for $0 < \Omega < 6.6$. Notice also in

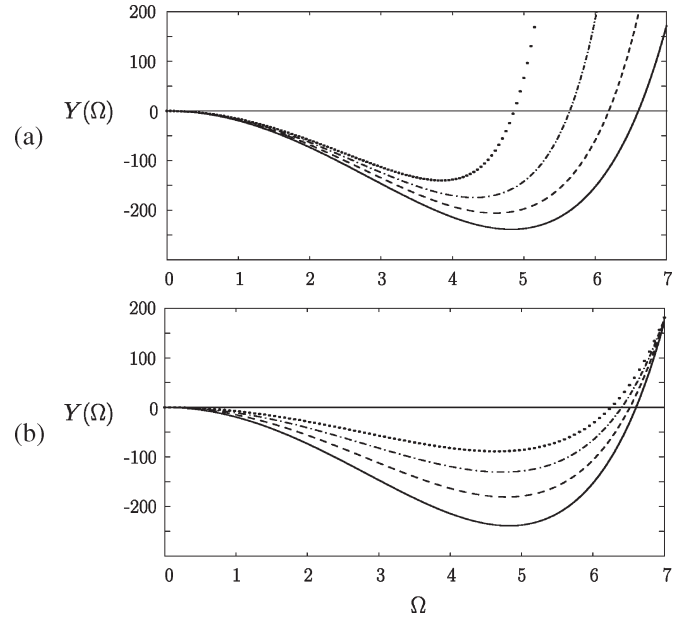


Fig. 5. Function $Y(\Omega)$ where the (a) ac excitation voltage is held constant at $V_A = 40$ V and dc tuning voltage is varied (solid: $V_0 = 75$ V; dashed: $V_0 = 70$ V; dashed-dotted: $V_0 = 65$ V; dotted: $V_0 = 60$ V) and (b) dc tuning voltage is held constant at $V_0 = 75$ V and ac excitation is varied (solid: $V_A = 40$ V; dashed: $V_A = 35$ V; dashed-dotted: $V_A = 30$ V; dotted: $V_A = 25$ V). When $Y(\Omega) < 0$, Melnikov's method predicts that an invariant chaotic set exists.

Fig. 5(a) that as V_0 decreases, the band of Ω for which chaos occurs decreases. A similar trend occurs when V_A is decreased, as shown in Fig. 5(b).

Next, knowing that Melnikov's method predicts that chaos can occur for a range of parameters, it becomes important to determine what type of chaos occurs, specifically whether transient (temporary) chaos, attracting (sustained) chaos, or both exist. This is done numerically by integrating (4) and studying the system's dynamics for a large number of parameter sets and initial conditions. Both attracting and transient chaos are found. Sustained chaos is the main interest in this paper, due to its impact in practical engineering applications. Fig. 6 depicts the system's phase space and time series for a set of parameters ($V_A = 40$ V, $V_0 = 75$ V, and $\Omega = 1.15$) where attracting chaos occurs. We determined that the chaos is sustained (attracting) by integrating the equations for 10^6 time units and verifying that the trajectories do not repeat.

Using the same voltages $V_A = 40$ V and $V_0 = 75$ V, numerical bifurcation analysis with Ω treated as the bifurcation parameter reveals the various transitions between periodic and chaotic states. Fig. 7(a) was constructed by beginning with $\Omega = 1.3$, adiabatically decreasing Ω , integrating for a sufficient amount of time at each step to remove transients, and recording the instantaneous value of z each time the trajectory pierced the Poincaré section defined by $\cos(\Omega\tau) = 0$ and $\sin(\Omega\tau) = 1$. The two panels in Fig. 7 represent different integration times at each Ω value. Due to the system's sensitive dependence on initial conditions, there are slight differences between the two panels. These differences also indicate that this system can have coexisting attractors for certain parameter sets, with only one shown for each Ω in each panel of Fig. 7. For $1.247 < \Omega < 1.300$ in Fig. 7(a), there is a stable periodic

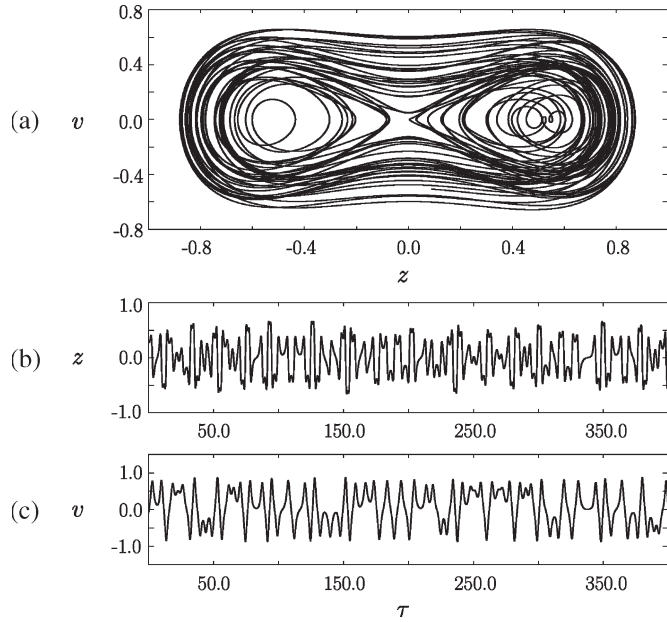


Fig. 6. Numerical simulations for $V_A = 40$ V, $V_0 = 75$ V, and $\Omega = 1.15$ showing attracting chaos in (a) (z, v) phase space, (b) z time series, and (c) v time series.

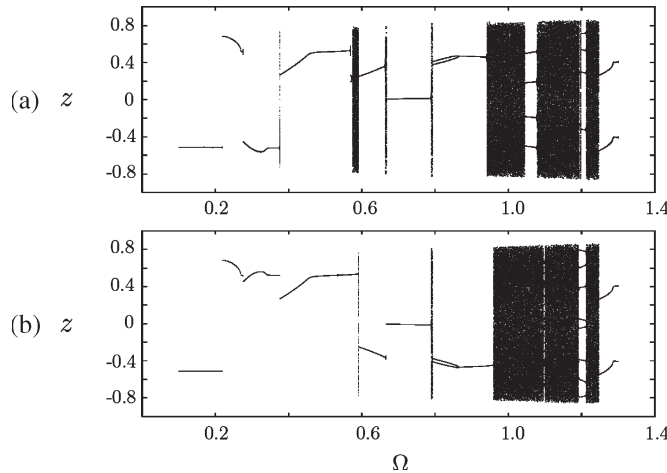


Fig. 7. Bifurcation diagrams obtained by setting $V_A = 40$ V and $V_0 = 75$ V and adiabatically decreasing the value of Ω from $\Omega = 1.300$ and omitting transients after integrating for a sufficient number of time units. Here, the instantaneous value of the nondimensionalized displacement z is plotted when the trajectory pierces the Poincaré section defined by $\cos(\Omega\tau) = 0$ and $\sin(\Omega\tau) = 1$. At each value of Ω , the equations are integrated for (a) 500 piercings of the Poincaré section and (b) 1500 piercings of the Poincaré section before omitting transients. This system contains multiple attractors at certain Ω values, but only one is depicted in each panel.

attractor with a period roughly two times that of the forcing. An abrupt transition to a chaotic state occurs at $\Omega = 1.247$, which is shown in the figure as a filled band. Within this chaotic region lies $\Omega = 1.15$, which is consistent with the results shown in Fig. 6. We verified that this is chaotic behavior by integrating (4) and observing the oscillations for Ω values that lie within these banded regions and by analyzing the Poincaré maps and power spectra of the system. There are three large banded chaotic regimes in the range $0.942 < \Omega < 1.246$, with small periodic windows in between, which indicate that there is a fairly large regime of parameter space for which this

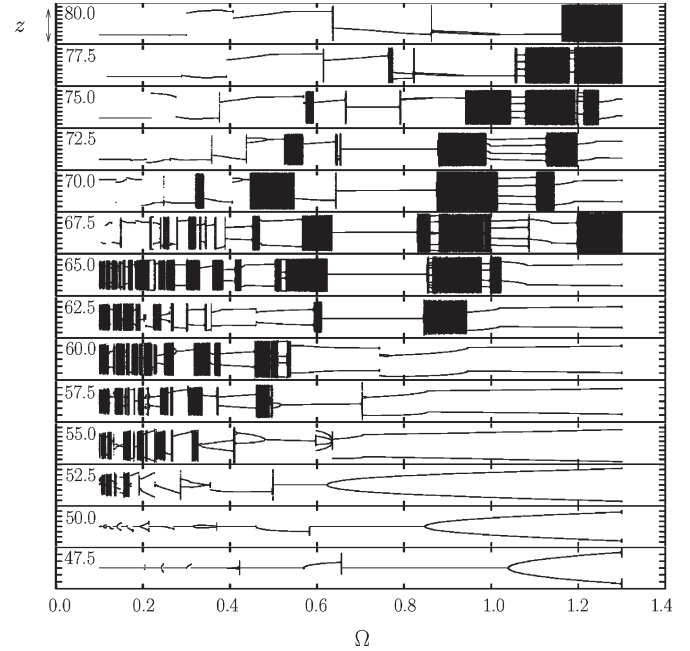


Fig. 8. Bifurcation diagrams similar to Fig. 7 ($V_A = 40$ V) stacked on top of one another for different dc tuning voltages V_0 , which are specified in the upper left-hand corner of each diagram. Evident from these plots is the relationship between the banded chaotic regions and the dc tuning voltage.

oscillator can exhibit attracting chaotic behavior; therefore, if an oscillator is created with parameters close to the ones shown in Table II, then chaotic behavior should be relatively easy to find by independently adjusting V_A , V_0 , and Ω . We note that qualitatively similar bifurcation diagrams have been computed for a different nonparametrically forced nonlinear oscillator in [25].

Holding $V_A = 40$ V, a series of bifurcation diagrams showing the dependence on V_0 was created in the same manner as Fig. 7; see Fig. 8 for 47.5 V $< V_0 < 80$ V. For $V_0 = 52.5$ V, which is just above $V_{0,\text{crit}}$ for $\beta < 0$, thick banded chaotic regions reside at low frequencies below $\Omega = 0.2$. As the dc voltage is increased, the chaotic bands become wider and spread into the higher frequency regions of parameter space. In a practical MEM device, it is likely that there will be an upper limit on the value of V_0 that the device can handle. For applications where chaos is desirable, such as signal encryption, when operating at lower dc tuning voltages chaos should be present at low frequencies relative to the natural frequency of the device.

V. EXPERIMENTAL VERIFICATION OF CHAOTIC BEHAVIOR

A MEM oscillator, which satisfies Melnikov's criterion for a range of applied ac and dc voltages, has been designed and fabricated. An SEM image of the device is shown in Fig. 1. Similar to the device discussed in Section IV, misaligned comb fingers were chosen for dc tuning, aligned comb fingers were chosen for actuation, and fixed-fixed flexures were chosen to provide the highly nonlinear mechanical restoring force. The dc tuning comb fingers were designed with a $2\text{-}\mu\text{m}$ width, $7\text{-}\mu\text{m}$ spacing, $1\text{-}\mu\text{m}$ gap, and $15\text{-}\mu\text{m}$ length. The ac driving comb fingers were designed with a slightly different geometry,

TABLE III
ESTIMATED PARAMETERS FOR THE EXPERIMENTAL DEVICE

k_1	$9.6 \mu\text{N}/\mu\text{m}$
k_3	$7.3 \mu\text{N}/\mu\text{m}^3$
m	$1.6 \times 10^{-9} \text{kg}$
Q	1558
r_{10}	$-4.7 \times 10^{-3} \mu\text{N}/(\text{V}^2 \mu\text{m})$
r_{30}	$1.8 \times 10^{-4} \mu\text{N}/(\text{V}^2 \mu\text{m}^3)$
r_{1A}	$1.1 \times 10^{-3} \mu\text{N}/(\text{V}^2 \mu\text{m})$
r_{3A}	$-1.4 \times 10^{-4} \mu\text{N}/(\text{V}^2 \mu\text{m}^3)$

specifically the comb fingers attached to the electrode were designed with a $3\text{-}\mu\text{m}$ width and comb fingers attached to the oscillator backbone were designed with a $2\text{-}\mu\text{m}$ width in order to increase the displacement range of the oscillator (there is an allowable displacement for aligned comb fingers, which if exceeded will cause the comb drive stiffnesses to change; they would become misaligned). In addition, the ac driving comb fingers were made to have $11\text{-}\mu\text{m}$ spacing, $1.5\text{-}\mu\text{m}$ gap, and $15\text{-}\mu\text{m}$ length. Each fixed–fixed flexure was designed with a $2\text{-}\mu\text{m}$ width and a $225\text{-}\mu\text{m}$ length, and the depth of the entire structure was $20 \mu\text{m}$. Parameters estimated through finite-element simulations are shown in Table III. Note that the value for Q in this table was estimated experimentally for the device in a 535 mtorr vacuum, which was the vacuum pressure used for all the results in this section. The pure elastic linear natural frequency was 9.2 kHz in the experiment, which differs slightly from the natural frequency estimated from the parameters in Table III (12.3 kHz). In all experiments, the driving frequency is less than the pure elastic linear natural frequency (corresponding to the lowest frequency vibration mode of the structure), so that other vibration modes do not contaminate the oscillator’s response.

Variations in parameters resulting from small imperfections in the fabricated structure will affect the onset of chaos according to (19). However, since parameters β and δ depend on V_0 and γ and η depends on V_A , the device can still be tuned to give chaos, and it is thus qualitatively insensitive to small parameter variations.

To test whether the device can achieve (11), a dc voltage was applied to the tuning set of comb fingers and was increased until it buckled to a new equilibrium position. This was done statically, and the relative position of the device was observed through a microscope. As seen in Fig. 9, the device’s stable equilibrium position, where the comb fingers are completely aligned, becomes unstable somewhere between $V_0 = 36.0 \text{ V}$ [Fig. 9(a)] and $V_0 = 36.5 \text{ V}$ [Fig. 9(b)], giving rise to a bifurcation where two new stable equilibria are born. The slight misalignment at 36.5 V shows that the system settled to one of the new stable equilibria positions. It is important to note that the device snaps to one of the two stable equilibria positions over the other due presumably to the presence of small fabrication-induced asymmetries that give rise to a distorted double-well potential. As the dc voltage was increased, for example to 37.0 V [Fig. 9(c)], the oscillator’s new equilibrium position moved further away from its original equilibrium position. This is consistent with the behavior of the system’s double-well potential when V_0 is increased. It is therefore concluded that

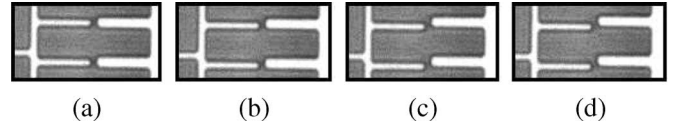


Fig. 9. Zoomed-in views of comb fingers (in each panel, the left two fingers are attached to the suspended structure and the right fingers are attached to the static electrode), depicting the transition to the buckled state where the effective linear stiffness is negative ($\beta < 0$) and the effective nonlinear stiffness is positive ($\delta > 0$). Here, a dc voltage is applied to the tuning set of comb fingers and no ac excitation is provided to the other set. Note that the comb fingers shown are originally aligned when no dc voltage is applied. (a) Comb fingers remain aligned for $V_0 = 36.0 \text{ V}$. (b) When $V_0 = 36.5 \text{ V}$, the structure buckles to one of two new equilibrium positions (i.e., $\beta < 0$ and $\delta > 0$), as shown by the slight misalignment of the fingers. (c), (d) As the voltage is increased, to $V_0 = 37 \text{ V}$ and $V_0 = 37.5 \text{ V}$ respectively, the fingers become more misaligned, which corresponds to the broadening of the double-well potential.

for dc tuning voltages above 36.5 V the oscillator’s phase space will have a homoclinic structure, with $\beta < 0$ and $\delta > 0$. Since $r_{30} > 0$, the $\delta > 0$ criterion will be satisfied for all V_0 .

To test the dynamical behavior of the oscillator in its buckled state, a vibrometer was used [26]. Since the motion of the device was in-plane with respect to the substrate, a 45° mirror was machined, with a focused ion beam, next to the proof mass so that the laser could be reflected off its vibrating surface. While applying a dc voltage to the tuning set of comb fingers, which was above the critical dc voltage, a square root cosine signal was applied to the driving comb fingers to actuate the device. For this experiment, there was an upper limit on the dc voltage that was determined by the spacing of the comb fingers. Since the oscillator displaces as V_0 is increased past $V_{0,\text{crit}}^\beta$, a point can be reached where the relative position of the noninterdigitated comb fingers causes the sign of the electrostatic stiffness coefficients to change (i.e., the misaligned fingers get closer to being aligned and visa versa), in which case a homoclinic orbit may no longer exist. From the force–displacement curve obtained from finite-element analysis, it was found that the misaligned tuning comb fingers could only displace $\pm 2.2 \mu\text{m}$ and the aligned driving comb fingers could only displace $\pm 1.8 \mu\text{m}$ before the sign of their respective stiffness coefficients changed. As a result, only a very narrow band of V_0 was explored.

Further evidence that the system contains a homoclinic structure comes from experimentally observed periodic attractors for different choices of V_0 , V_A , and ω . Before proceeding, it is important to note that the vibrometer integrates the velocity measurement to obtain the displacement, so there was some drift associated with the experimental displacement values. As a result, the displacement results have some amount of offset so that zero displacement does not correspond to the original equilibrium position. Fig. 10 shows an experimentally observed periodic attractor for $V_0 = 37.1 \text{ V}$, $V_A = 13.2 \text{ V}$, and a driving frequency of 1100 Hz , and Fig. 11(a) shows a different experimentally observed periodic attractor for $V_0 = 37.1 \text{ V}$, $V_A = 14.8 \text{ V}$, and a driving frequency of 1500 Hz . The shapes of these periodic orbits in phase space are consistent with a system that contains homoclinic trajectories for $\epsilon = 0$ [23]. Fig. 11(b) shows a periodic attractor found numerically for the parameters in Table III, with $V_0 = 47 \text{ V}$, $V_A = 15.9 \text{ V}$, and a driving frequency of 1500 Hz . This strongly resembles

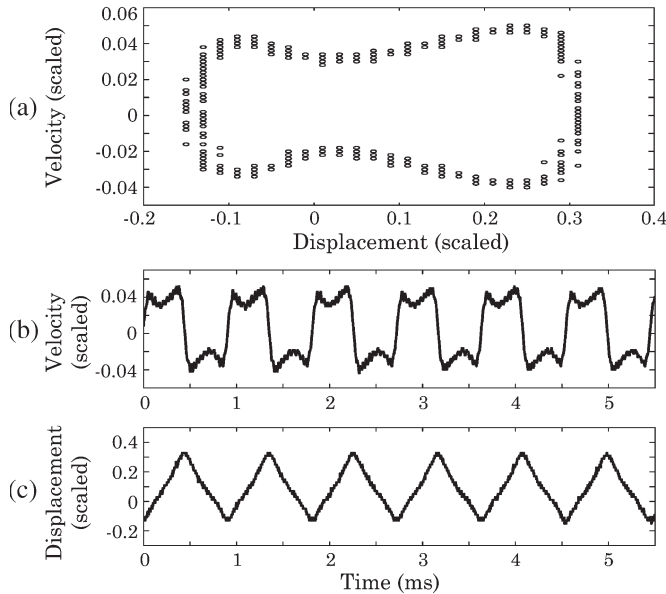


Fig. 10. Periodic attractor for the experimental device for $V_0 = 37.1$ V, $V_A = 13.2$ V, $\omega/2\pi = 1100$ Hz, with the (a) phase space, (b) velocity time series, and (c) displacement time series shown [1 velocity (scaled) unit = 125 mm/s and 1 displacement (scaled) unit = $8 \mu\text{m}$].

the periodic orbit shown in Fig. 11(a), although, interestingly, the period of the periodic orbit shown in Fig. 11(a) is twice the period of the driving signal, while the period of the periodic orbit shown in Fig. 11(b) (and that shown in Fig. 10) is equal to the period of the driving signal.

In addition to finding numerous periodic attractors, regions of (V_A, V_0, ω) parameter space where attracting chaos occurs were found. For example, when $V_0 = 37.1$ V, $V_A = 13.8$ V, and $\omega/2\pi = 2000$ Hz, a chaotic attractor was found experimentally, with a time series shown in Fig. 12(a). Using the parameters from Table III and those near V_A, V_0 , and ω , attracting chaos was found numerically, as shown in Fig. 12(b). To verify that the chaos is sustained, the equations were integrated for 10^6 time units. We note that here the experimental device was tested at $V_0 = 37.1$ V, which is slightly above its critical dc tuning voltage. Since the predicted parameters in Table III are not expected to be exactly the same as those for the device due to fabrication issues, the critical dc tuning voltage for homoclinic orbits to occur is different. The transition voltage for the parameters in Table III is $V_{0,\text{crit}}^\beta = 45.2$ V. To be consistent with the experiment, a value of $V_0 = 46.5$ V, which is slightly above this theoretical prediction, was chosen for the simulation shown in Fig. 12(b).

Spectral analysis of an oscillator's time series is a good indicator of whether it is chaotic [27]. This was done here by taking the Fourier transform of the time series obtained experimentally and numerically with the same V_A, V_0 , and ω as in Fig. 12. The power spectrum was found by taking the modulus of the Fourier transform, and it determines the relative strength of each periodic component in the time series. In general, systems whose time series are chaotic will have a broad power spectrum. Fig. 13(a) shows such a broad power spectrum for the actual device, suggesting chaotic oscillations for these parameters. Fig. 13(b) shows a similarly broad power spectrum from numer-

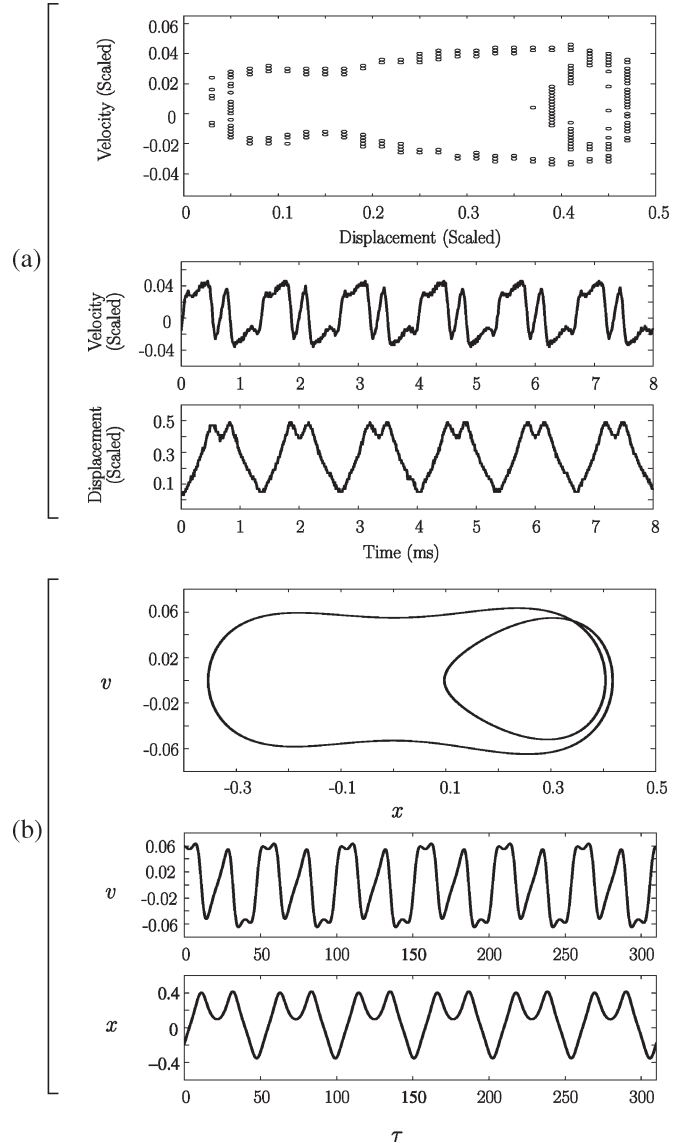


Fig. 11. Comparison of a periodic attractor obtained in the (a) experiment for $V_0 = 37.1$ V, $V_A = 14.8$ V, and $\omega/2\pi = 1500$ Hz [1 velocity (scaled) unit = 125 mm/s and 1 displacement (scaled) unit = $8 \mu\text{m}$] and (b) numerical simulation for $V_0 = 47.0$ V, $V_A = 15.9$ V, and $\omega/2\pi = 1500$ Hz.

ical simulations. The peak of the experimental power spectrum is apparently at half the driving frequency (although there is also substantial power at the driving frequency), whereas the peak of the numerical power spectrum is apparently at the driving frequency (although there is also substantial power at half the driving frequency). This suggests that the experimental and numerical chaotic oscillations are quite similar but differ somewhat in their details.

For the estimated parameter set in Table III and fixed V_0 , a boundary was derived from (19) in $\omega-V_A$ space, which predicts where chaos occurs (above the curves). For comparison, this boundary was also tested experimentally. This was done by fixing $V_0 = 37.0$ V, increasing V_A until attracting chaotic behavior was observed, and recording this V_A every 50 Hz. For this experiment, the device was only tested for V_A below 25.0 V, since similar devices failed for voltages slightly above this value. No chaos was observed for frequencies past 3300 Hz

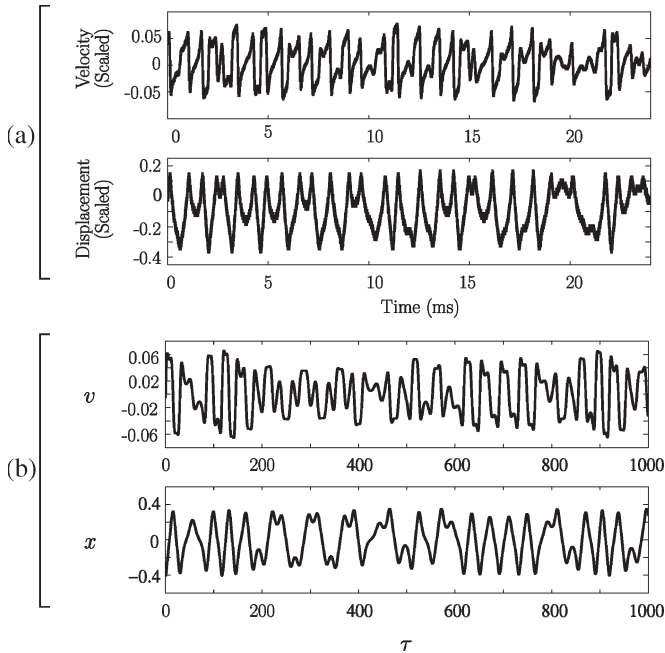


Fig. 12. Comparison of a chaotic time series obtained in the (a) experiment for $V_0 = 37.1$ V, $V_A = 13.8$ V, and $\omega/2\pi = 2000$ Hz [1 velocity (scaled) unit = 125 mm/s and 1 displacement (scaled) unit = $8 \mu\text{m}$] and (b) numerical simulation for $V_0 = 46.5$ V, $V_A = 15.0$ V, and $\omega/2\pi = 2010$ Hz.

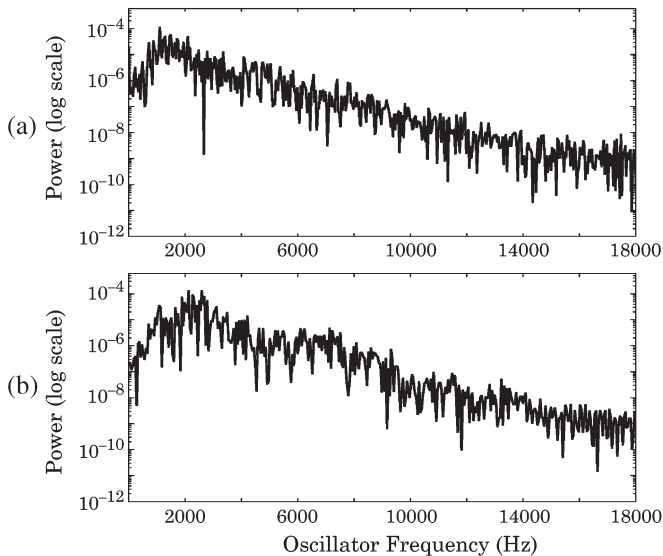


Fig. 13. Power spectra calculated by taking the Fourier transform of a chaotic velocity time series from (a) experiment ($V_0 = 37.1$ V, $V_A = 13.8$ V, and $\omega/2\pi = 2000$ Hz) and (b) numerical analysis ($V_0 = 46.5$ V, $V_A = 15.0$ V, and $\omega/2\pi = 2010$ Hz), showing the broad-band nature of the chaotic attractor [the scaled velocity units prior to taking the Fourier transform are identical to Fig. 12 for (a) and (b)].

since the drive voltage necessary to achieve chaotic behavior becomes too large. The boundary for attracting chaotic behavior found in the experiment lies above the theoretical boundaries for the existence of a chaotic set predicted by Melnikov's method, as shown in Fig. 14. The gap between the theoretical and experimental curves could be due to the fact that the chaos predicted by Melnikov's method could be transient or attracting, and we only show the experimental boundary for attracting chaos.

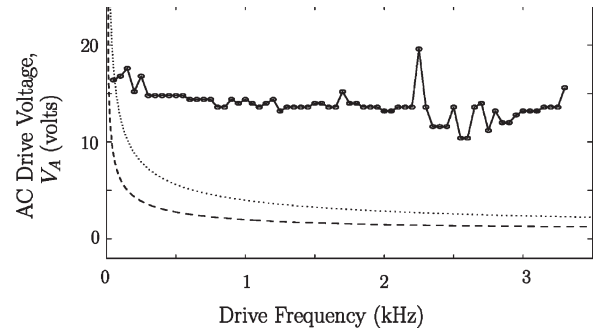


Fig. 14. Boundaries for chaotic motion in ac drive voltage versus drive frequency space. Above the experimental curve (solid curve), attracting chaos exists ($V_0 = 37.0$ V), and above the curves predicted by Melnikov's method (dashed curve: $V_0 = 47.0$ V and dotted curve: $V_0 = 37.0$ V), chaotic motion, which could be transient or attracting, is possible.

VI. CONCLUSION

Using Melnikov's method, chaos has been predicted to occur in MEM oscillators that are governed by a version of the Mathieu equation that includes both linear and nonlinear time-dependent stiffness terms. The result of this analysis was an inequality describing the set of parameters where chaos occurs, which is a useful design tool for tailoring the oscillator's parameters so homoclinic chaos either occurs or does not occur as desired. For a representative parameter set, numerical simulations showed that chaos does occur in regions of parameter space satisfying the criterion from Melnikov's method and helped to better understand the complicated dynamics of the oscillator. A MEM oscillator with two sets of noninterdigitated comb drives (one for ac actuation and one for dc tuning) was designed and fabricated so that it satisfies Melnikov's criterion for a region of parameter space. By tuning the device with the dc comb drives, the effective linear and nonlinear stiffnesses are made to be negative and positive, respectively, which means that the unperturbed system contains a homoclinic orbit. By actuating the device with the second set of electrodes, many interesting attractors are found, including periodic orbits and chaos. Time series and broad-band spectra observed experimentally show that the MEM device is chaotic for appropriate parameters and that the criterion from Melnikov's method is valid for predicting chaotic behavior.

ACKNOWLEDGMENT

The authors would like to thank the anonymous referees for useful suggestions that helped improve this paper. The authors would also like to thank S. Shaw and J. Rhoads for informative discussions and L. Oropeza for taking the SEM image shown.

REFERENCES

- [1] S. Shaw, K. Turner, J. Rhoads, and R. Baskaran, "Parametrically excited MEMS-based filters," in *Proc. IUTAM Symp. Chaotic Dyn. Control Syst. Process.*, 2003, vol. 122, pp. 137–146.
- [2] J. Rhoads, S. Shaw, K. Turner, and R. Baskaran, "Tunable MEMS filters that exploit parametric resonance," *J. Vib. Acoust.*, vol. 127, no. 5, pp. 423–430, Oct. 2005.
- [3] W. Zhang, R. Baskaran, and K. Turner, "Effect of cubic nonlinearity on auto-parametrically amplified resonant MEMS mass sensor," *Sens. Actuators A, Phys.*, vol. 102, no. 1/2, pp. 139–150, Dec. 2002.

- [4] M. Requa and K. Turner, "Electromechanically driven and sensed parametric resonance in silicon microcantilevers," *Appl. Phys. Lett.*, vol. 88, no. 26, pp. 263508.1–263508.3, Jun. 2006.
- [5] K. Turner, S. Miller, P. Hartwell, N. MacDonald, S. Strogatz, and S. Adams, "Five parametric resonances in a microelectromechanical system," *Nature*, vol. 396, no. 6707, pp. 149–152, Nov. 1998.
- [6] J. Rhoads, S. Shaw, K. Turner, J. Moehlis, B. DeMartini, and W. Zhang, "Generalized parametric resonance in electrostatically-actuated microelectromechanical oscillators," *J. Sound Vib.*, vol. 296, no. 4/5, pp. 797–829, Oct. 2006.
- [7] B. DeMartini, J. Moehlis, K. Turner, J. Rhoads, S. Shaw, and W. Zhang, "Modeling of parametrically excited microelectromechanical oscillator dynamics with application to filtering," in *Proc. IEEE Sens. Conf.*, Irvine, CA, 2005, pp. 345–348.
- [8] G. Abraham and A. Chatterjee, "Approximate asymptotics for a nonlinear Mathieu equation using harmonic balance based averaging," *Nonlinear Dyn.*, vol. 31, no. 4, pp. 347–365, Mar. 2003.
- [9] R. Zounes and R. Rand, "Subharmonic resonance in the non-linear Mathieu equation," *Int. J. Non-Linear Mech.*, vol. 37, no. 1, pp. 43–73, Jan. 2002.
- [10] S. Adams, F. Bertsch, and N. MacDonald, "Independent tuning of linear and nonlinear stiffness coefficients," *J. Microelectromech. Syst.*, vol. 7, no. 2, pp. 172–180, Jun. 1998.
- [11] W. Zhang, R. Basharan, and K. Turner, "Tuning the dynamic behavior of parametric resonance in a micromechanical oscillator," *Appl. Phys. Lett.*, vol. 82, no. 1, pp. 130–132, Jan. 2003.
- [12] B. DeMartini, J. Rhoads, K. Turner, S. Shaw, and J. Moehlis, "Linear and nonlinear tuning of parametrically excited MEMS oscillators," *J. Microelectromech. Syst.*, vol. 16, no. 2, pp. 310–318, Apr. 2007.
- [13] E. Lorenz, "Deterministic nonperiodic flow," *J. Atmos. Sci.*, vol. 20, no. 2, pp. 130–141, Mar. 1963.
- [14] M. Basso, L. Giarré, M. Dahleh, and I. Mezić, "Numerical analysis of complex dynamics in atomic force microscopes," in *Proc. IEEE Int. Conf. Control Appl.*, Trieste, Italy, Sep. 1–4, 1998, pp. 1026–1030.
- [15] M. Ashhab, M. Salapaka, M. Dahleh, and I. Mezić, "Melnikov-based dynamical analysis of microcantilevers in scanning probe microscopy," *Nonlinear Dyn.*, vol. 20, no. 3, pp. 197–220, Nov. 1999.
- [16] M. Ashhab, M. Salapaka, M. Dahleh, and I. Mezić, "Dynamical analysis and control of microcantilevers," *Automatica*, vol. 35, no. 10, pp. 1663–1670, Oct. 1999.
- [17] S. Hu and A. Raman, "Chaos in atomic force microscopy," *Phys. Rev. Lett.*, vol. 96, no. 3, p. 036107, Jan. 2006.
- [18] F. Jamitzky, M. Stark, W. Bunk, W. Heckl, and R. Stark, "Chaos in dynamic atomic force microscopy," *Nanotechnology*, vol. 17, no. 7, pp. S213–S220, Apr. 2006.
- [19] Y. Wang, S. Adams, J. Thorp, N. MacDonald, P. Hartwell, and F. Bertsch, "Chaos in MEMS, parameter estimation and its potential application," *IEEE Trans. Circuits Syst. I, Fundam. Theory Appl.*, vol. 45, no. 10, pp. 1013–1020, Oct. 1998.
- [20] S. Liu, A. Davidson, and Q. Lin, "Simulation studies on nonlinear dynamics and chaos in a MEMS cantilever control system," *J. Micromech. Microeng.*, vol. 14, no. 7, pp. 1064–1073, Jul. 2004.
- [21] A. Luo and F. Wang, "Nonlinear dynamics of a micro-electro-mechanical system with time-varying capacitors," *J. Vib. Acoust.*, vol. 126, no. 1, pp. 77–83, Jan. 2004.
- [22] S. K. De and N. Aluru, "Complex oscillations and chaos in electrostatic microelectromechanical systems under superharmonic excitations," *Phys. Rev. Lett.*, vol. 94, no. 20, pp. 204101.1–204101.4, May 2005.
- [23] J. Guckenheimer and P. Holmes, *Nonlinear Oscillations, Dynamical Systems, and Bifurcations of Vector Fields*. New York: Springer-Verlag, 1983.
- [24] S. Wiggins, *Introduction to Applied Nonlinear Dynamical Systems and Chaos*, 2nd ed. New York: Springer-Verlag, 2003.
- [25] A. Venkatesan and M. Lakshmanan, "Bifurcation and chaos in the double-well Duffing–Van der Pol oscillator: Numerical and analytical studies," *Phys. Rev. E, Stat. Phys. Plasmas Fluids Relat. Interdiscip. Top.*, vol. 56, no. 6, pp. 6321–6330, Dec. 1997.
- [26] K. Turner, P. Hartwell, and N. MacDonald, "Multi-dimensional MEMS motion characterization using laser vibrometry," in *Proc. Transducers 10th Int. Conf. Solid-State Sens., Actuators*, 1999, pp. 1144–1147.
- [27] F. Moon, *Chaotic Vibrations: An Introduction for Applied Scientists and Engineers*. Toronto, ON, Canada: Wiley-Interscience, 1987.



Barry E. DeMartini (S'05) received the B.S. degree in mechanical engineering in 2003 from the University of California, Santa Barbara, where he is currently working toward the Ph.D. degree in mechanical engineering.

His research interests include novel resonant mass sensors for chemical and biological detection, design and characterization of micro/nanoscale resonators, and nonlinear dynamics and chaos in microelectromechanical systems.

Mr. DeMartini is a student member of the Society for Industrial and Applied Mathematics.



Holly E. Butterfield received the B.S. degree in mechanical engineering from the University of California, Santa Barbara. She is currently working toward an M.S. degree in mechanical engineering at Stanford University, CA.

Her research interests include nonlinear dynamics and sensing in MEMS.

Ms. Butterfield is a Student Member of the American Society of Mechanical Engineers and a member of Tau Beta Pi.



Jeff Moehlis received the B.S. degree in physics and mathematics from Iowa State University, Ames, in 1993, and the Ph.D. degree in physics from the University of California, Berkeley, in 2000.

He was a Postdoctoral Researcher in the Program in Applied and Computational Mathematics with Princeton University, Princeton, NJ, from 2000 to 2003. He is currently an Associate Professor of mechanical engineering with the Department of Mechanical Engineering, University of California, Santa Barbara, where he has served on the faculty since

2003. His research interests include dynamical systems and their application to neuroscience, turbulence, MEMS devices, and fish schooling.

Dr. Moehlis was a recipient of a Sloan Research Fellowship in Mathematics and the National Science Foundation CAREER Award.



Kimberly L. Turner (M'02) received the B.S. degree in mechanical engineering from Michigan Technological University, Houghton, in 1994, and the Ph.D. degree in theoretical and applied mechanics from Cornell University, Ithaca, NY, in 1999.

She is currently an Associate Professor of mechanical engineering with the Department of Mechanical Engineering, University of California, Santa Barbara, where she has served on the faculty since 1999. Her research interests include nonlinear dynamics of micro/nanoscale systems, testing and characterization of MEMS devices, modeling of micro/nanoscale devices, and solid-state sensor development.

Dr. Turner is a member of the American Society of Mechanical Engineers, Society for Experimental Mechanics, American Vacuum Society (AVS), and the Cornell Society of Engineers. She was a recipient of the National Science Foundation CAREER Award and the Varian Award from the AVS.